References and Notes

1. D. J. Wald, T. H. Heaton, *Bull. Seismol. Soc. Am.* **84**, 668 (1994).
2. D. P. Hill *et al.*, *Science* **260**, 1617 (1993).
3. P. Bodin, J. Gomberg, *Bull. Seismol. Soc. Am.* **84**, 835 (1994).
4. R. S. Stein, G. C. P. King, J. Lin, *Science* **258**, 1328 (1992).
5. The Coulomb failure stress change $\Delta\sigma_f = \Delta\tau - \mu(\Delta\sigma_n - \Delta\Pi)$, where $\Delta\tau$ is the shear stress change resolved into the fault plane, $\Delta\sigma_n$ is the stress change perpendicular to the fault plane (positive toward the plane), μ is the coefficient of friction, and $\Delta\Pi$ is the pore pressure, measures the change of stress on preexisting faults that is due to a redistribution of stress by a major tectonic event. Increasing τ or reducing σ_n advances the probability of failure. This probability is also increased if a reduction of τ is accompanied by an even larger reduction in σ_n. The free parameters of the model are (i) orientation of the local fault plane, (ii) details of the geometry of the main rupture, (iii) orientation of the regional stress field (in the case of choosing planes with optimal orientation), (iv) μ, and (v) Π. We suggest that these parameters are poorly known, with margins of error that allow adjustments, such that the observed seismicity rate changes are correctly modeled. We view the quantitatively established pattern of increased and decreased seismicity as a solid observation that may help constrain the model along with other data, such as the measurements of surface deformations near the mainshock.
6. S. Wiemer, M. Wyss, *Bull. Seismol. Soc. Am.* **84**, 900 (1994).
7. Scientists from the U.S. Geological Survey, Southern California Earthquake Center, and California Division of Mines and Geology, *Seismol. Res. Lett.* **71**, 11 (2000).
8. The analysis reported was performed on the declustered [P. A. Reasenberg, *J. Geophys. Res.* **90**, 5479 (1985)] data set because the estimate of the background values of *a*′ and *b* should not be contaminated by aftershocks and swarms. However, we also performed all analyses using the full data set, including aftershocks. We found that the results do not depend on the inclusion or exclusion of clusters.
9. The homogeneity of reporting earthquakes over decades and as a function of space is a thorny question that we have investigated in detail before conducting seismicity studies [F. R. Zuniga, M. Wyss, *Bull. Seismol. Soc. Am.* **85**, 1858 (1995); F. R. Zuniga, S. Wiemer, *Pure Appl. Geophys.* **153**, 713 (1999)]. In general, most reported rate changes are due to artificial causes, and we have developed criteria by which some of these can be identified. We examined the earthquake catalog for southern California (Southern California Earthquake Center) by the GENAS algorithm [R. E. Habermann, *J. Geophys. Res.* **88**, 5056 (1983)] and found that it is of high quality since 1981, but does contain some changes that may be artificial. The changes we report here do not conform to patterns of known artificial changes; they coincide with the time of the Landers earthquake, and they have opposite signs (increase and decrease in neighboring volumes). Therefore, these changes are likely of natural origin. In addition, we deleted small volumes that contained a strong preponderance of daytime events from the analysis, because these are most likely explosions.
10. S. Wiemer, thesis, University of Alaska, Fairbanks (1996).
11. Instead of reporting percentages of rate changes, which could be large but statistically insignificant, we estimate the statistical significance of the rate change at a given time t_c by the standard deviate *Z* test, $Z = (\mu_2 - \mu_1)/(S_1/n_1 + S_2/n_2)^{1/2}$. The larger the difference between the two means, μ, and the larger the numbers of samples, *n*, before and after t_c (index 1 and 2, respectively), the more confidence one can place in the significance of a difference, whereas large variances of the means, *S*, decrease the confidence.
12. T. Utsu, in *Report of the Joint Research Institute for Statistical Mathematics* (Institute for Statistical Mathematics, Tokyo, 1992), vol. 34, pp. 139–157.
13. D. Marriott, S. Hreinsdottir, M. Wyss, *Eos* **81**, S302 (2000).
14. T. Parsons, D. S. Dreger, *Geophys. Res. Lett.* **27**, 1949 (2000).
15. Recently, we have shown that the *b* value is not as constant ($b \approx 1$) as previously thought [C. Frohlich, S. Davis, *J. Geophys. Res.* **98**, 631 (1993); Y. Y. Kagan, *Pure Appl. Geophys.* **155**, 537 (1999)] and can vary between 0.5 and 1.5 along fault zones [S. Wiemer, M. Wyss, *J. Geophys. Res.* **102**, 15115 (1997); Y. Ogata, K. Katsura, *Geophys. J. Int.* **113**, 727 (1993); F. Amelung, G. King, *Geophys. Res. Lett.* **24**, 507 (1997)]. We tested the hypothesis that asperities, the crucial hard spots that control main ruptures, may be mapped by minima in *b* values and in T_L values [M. Wyss, D. Schorlemmer, S. Wiemer, *J. Geophys. Res.* **105**, 7829 (2000)]. Thus, asperities seem to be locations that produce more medium-sized earthquakes, relative to small ones, than does the normal crust.
16. K. Aki, *Bull. Earthquake Res. Inst.* **43**, 237 (1965).
17. Increasingly detailed earthquake catalogs reveal that, beneath volcanoes, volumes surrounding the magma chambers produce far more small earthquakes ($b = 1.5$) than does the rest of the crust [(*41*); S. Wiemer, S. McNutt, *Geophys. Res. Lett.* **24**, 189 (1997); M. Murru, C. Montuori, M. Wyss, E. Privitera, *Geophys. Res. Lett.* **26**, 2553 (1999)] and that temporal changes of *b* values occur during intrusions [(*41*); M. Wyss, K. Shimazaki, S. Wiemer, *J. Geophys. Res.* **102**, 20413 (1997)].
18. The seismic hazard is usually expressed in expected ground acceleration, which is calculated on the basis of *P*, using attenuation laws and source zone definitions, as well as long historic earthquake catalogs. In addition, some national efforts of mapping the seismic hazard include information on crustal deformation. On occasion, attempts are made to estimate the time-dependent hazard, by also considering the occurrence time of the last large earthquakes on prominent faults. Here, we focus exclusively on the element of hazard assessment brought in by the turning on and off of seismicity due to stress redistribution by major ruptures.
19. S. J. Gross, C. Kisslinger, *J. Geophys. Res.* **102**, 7603 (1997).
20. D. D. Bowman, G. Ouillon, C. G. Sammis, A. Sornette, D. Sornette, *J. Geophys. Res.* **103**, 24359 (1998).
21. N. Kato, M. Ohtake, T. Hirasawa, *Pure Appl. Geophys.* **150**, 249 (1997).
22. M. Wyss, A. H. Martyrosian, *Geophys. J. Int.* **134**, 329 (1998).
23. M. Wyss, A. Hasegawa, S. Wiemer, N. Umino, *Ann. Geophys.* **42**, 851 (1999).
24. M. Wyss, S. Wiemer, *Pure Appl. Geophys.* **153**, 259 (1999).
25. L. M. Jones, E. Hauksson, *Geophys. Res. Lett.* **24**, 469 (1997).
26. D. J. Varnes, *Pure Appl. Geophys.* **130**, 661 (1989).
27. S. Jaume, L. R. Sykes, *Pure Appl. Geophys.* **155**, 279 (1999).
28. C. G. Sammis, S. W. Smith, *Pure Appl. Geophys.* **155**, 307 (1999).
29. C. H. Scholz, *Bull. Seismol. Soc. Am.* **58**, 399 (1968).
30. M. Wyss, *Geophys. J. R. Astron. Soc.* **31**, 341 (1973).
31. T. I. Urbancic, C. I. Trifu, J. M. Long, R. P. Young, *Pure Appl. Geophys.* **139**, 449 (1992).
32. J. Boatwright, M. Cocco, *J. Geophys. Res.* **101**, 13895 (1996).
33. D. Kilb, J. Gomberg, P. Bodin, *Nature*, in press.
34. E. Richardson, C. Marone, *J. Geophys. Res.* **104**, 28859 (1999).
35. T. Parsons, R. S. Stein, R. W. Simpson, P. A. Reasenberg, *J. Geophys. Res.* **104**, 20183 (1999).
36. R. S. Stein, *Nature* **402**, 605 (1999).
37. P. A. Reasenberg, R. W. Simpson, *U.S. Geol. Surv. Prof. Pap.* **1550-D**, D49 (1997).
38. V. I. Keilis-Borok, L. Knopoff, I. Rotwain, C. R. Allen, *Nature* **335**, 690 (1988).
39. L. Knopoff, T. Levshina, V. I. Keilis-Borok, C. Mattoni, *J. Geophys. Res.* **101**, 5779 (1996).
40. F. Press, C. Allen, *J. Geophys. Res.* **100**, 6421 (1995).
41. S. Wiemer, S. R. McNutt, M. Wyss, *Geophys. J. Int.* **134**, 409 (1998).

42. We thank M. Gerstenberger, C. Sammis, and three anonymous reviewers for comments on the manuscript. This research was supported by NSF grant EAR 9902717. This paper is contribution number 1151 of the Geophysical Institute, Eidgenössische Technische Hochschule, Zürich.

21 July 2000; accepted 4 October 2000

Sediments at the Top of Earth's Core

Bruce A. Buffett,[1]* Edward J. Garnero,[2] Raymond Jeanloz[3]

Unusual physical properties at the core-mantle boundary have been inferred from seismic and geodetic observations in recent years. We show how both types of observations can be explained by a layer of silicate sediments, which accumulate at the top of the core as Earth cools. Compaction of the sediments expels most of the liquid iron but leaves behind a small amount of core material, which is entrained in mantle convection and may account for the isotopic signatures of core material in some hot spot plumes. Extraction of light elements from the liquid core also enhances the vigor of convection in the core and may increase the power available to the geodynamo.

The boundary between Earth's liquid iron core and silicate mantle coincides with a region of unusual structural complexity (*1*). Strong lateral variations in *P*- and *S*-wave velocity are evident in the lowermost 200 km of the mantle (*2–5*). More substantial anomalies in the seismic velocities, possibly in excess of −10% (relative to the average seismic velocities in the lowermost mantle), have been detected within a few tens of kilometers of the core-mantle boundary (CMB) in several regions (*6–9*). These ultralow-velocity zones (ULVZs) have been interpreted as evidence for partial melt (*10*), although alterna-

[1]Department of Earth and Ocean Sciences, University of British Columbia, Vancouver, British Columbia V6T 1Z4, Canada. [2]Department of Geological Sciences, Arizona State University, Tempe, AZ 85287, USA. [3]Department of Earth and Planetary Science, University of California, Berkeley, CA 94720, USA.

*To whom correspondence should be addressed. E-mail: buffet@eos.ubc.ca

tive interpretations are possible (*11*).

Other indications of unusual physical properties are inferred from periodic variations (nutations) in Earth's rotation (*12*). Anomalous dissipation in the annual nutation can be explained by the effects of metallic electrical conductivities in the lowermost 200 m of the mantle (*13, 14*). Additional support for a conducting layer is derived from improving estimates of the 18.6-year nutation (Fig. 1A). These observations impose a key constraint on the structure of the CMB because the inferred electrical conductivity cannot be reconciled with the properties of silicates (*15*). Here, we explore the possibility that these anomalous features are caused by an accumulation of sediments at the CMB.

Estimates of density in the core suggest that the core is composed of Fe and lighter alloying components (*16*). It is generally thought that the components lighter than Fe were dissolved into the liquid iron during core formation (*17*), although the identity of the lighter elements is unknown. After the core forms, the liquid in contact with the base of the mantle evolves toward a chemical equilibrium, probably through chemical reactions between the silicates and the liquid iron (*18–20*). Vigorous convection in the core can thoroughly stir the liquid in 10^3 years (*21*), whereas changes in the structure of the mantle occur over 10^8 years. Thus, the liquid core should chemically equilibrate with the base of the mantle, although the composition of the silicate minerals in contact with the core may not be representative of the bulk of the mantle (*22*). Indeed, the mineral composition may not be uniform over the surface of the CMB.

Cooling and solidification of the core disturbs the chemical equilibrium by segregating lighter elements into the liquid outer core as the solid inner core grows (Fig. 2). The natural tendency to restore equilibrium with the base of the mantle should not be impeded by kinetic effects because of the high temperature (4000 ± 500 K) at the CMB (*23, 24*). We assume that chemical equilibrium is reestablished by precipitating lighter elements from the liquid core, although the form of the precipitate depends on the details of the equilibration process. Speculations about this process are guided by experiments on mixtures of perovskite and Fe at high pressure and temperature (*22*), which suggest that chemical reactions of the form

$$(Mg_y,Fe_{1-y})SiO_3 + 3(1-y)Fe \rightarrow y MgSiO_3 + (1-y)FeSi + 3(1-y)FeO \quad (1)$$

are possible at the pressure and temperature of the CMB. Here y denotes the mole fraction of Mg in the initial perovskite.

The segregation of FeSi and FeO into the liquid core by inner-core growth causes their concentrations to increase above the equilibrium concentrations with respect to the mantle. Under these conditions we expect the direction of the reaction to reverse, removing excess FeSi and FeO from the liquid core to form a silicate perovskite. Alternatively, the excess Si or O may precipitate as either a liquid or solid phase of an Fe-rich species. Deposition of a metallic solid phase poses some difficulties, because observations of short-period variations in the internal magnetic field limit the magnetic diffusion time of the mantle to less than a few years (*25*). Accumulation of a metallic layer in excess of 10 km would be sufficient to violate this observational constraint if the layer covered most of the CMB. Alternatively, a liquid phase may separate and pond at the boundary, but such a layer is unable to explain the unusual properties inferred at the CMB from seismic and geodetic observations. Consequently, we favor an equilibration mechanism that relies on chemical reactions. For the purposes of our calculations, we suppose that 1 mol of Fe alloy reacts to form 1 mol of silicate. The Fe alloy has the generic form FeX, and we consider several possible choices for the light element X. The resulting silicate is assumed to have the density, volume, and elastic properties of the average lower mantle (*26*).

We quantify the mass of light element X that precipitates from the liquid core under the assumption that convection keeps the liquid core well mixed. For chemical equilibrium to be maintained between the fluid core and the base of the mantle, the mass of X that precipitates from the fluid core must (on average) equal the mass of X that is rejected from the volume of the inner core. For simplicity, we assume a constant density ρ_c in the core, so the mass of X excluded from the inner core is given by $M_X = \Delta C M_{ic}$, where ΔC is the change in the mass fraction of X across the inner to outer core boundary and M_{ic} is the mass of the inner core. In our proposed chemical reaction, 1 mol of X (with molar mass m_X) is converted to 1 mol of silicate (with molar mass m_{sed}). It follows that the mass of the silicate sediment is $M_{sed} = (m_{sed}/m_X)M_X$.

Silicate minerals should accumulate at the top of the core because of their buoyancy in liquid Fe (*27*). Knowledge of where the sediments form and how they are deposited is

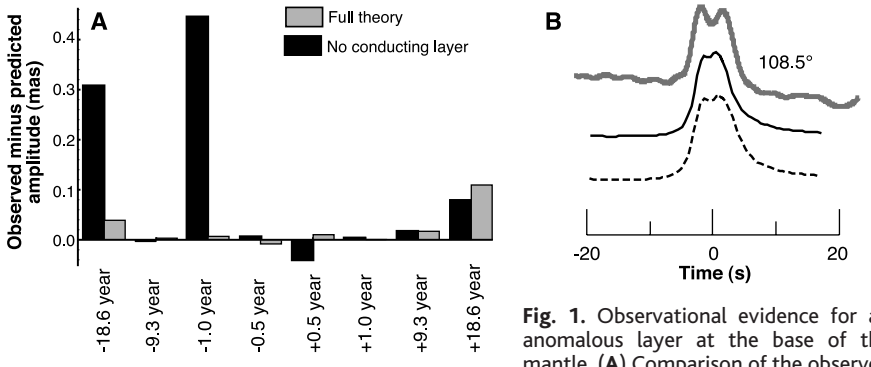

Fig. 1. Observational evidence for an anomalous layer at the base of the mantle. (**A**) Comparison of the observed and predicted nutations at the principal periods reveals two large discrepancies in the (out-of-phase) amplitudes of the –18.6-year and –1.0-year terms when a conducting layer is not included in the prediction (*42*). The amplitudes are measured in milliarcseconds (mas), and the sign of the period distinguishes prograde (+) and retrograde (–) motions. Including a thin layer with a conductance of 10^8 S significantly reduces these discrepancies relative to the measurement uncertainty of ±0.015 mas. (**B**) A broadband displacement record at 108.5° in distance (thick gray trace) is compared with two synthetic waveforms. Predictions using the physical properties of the sedimentary layer (solid line) are comparable to those obtained with a typical ULVZ model (dashed line), in which the layer thickness is 5 km and the velocity reductions in *P*- and *S*-wave velocities are –10% and –30%, respectively (see text).

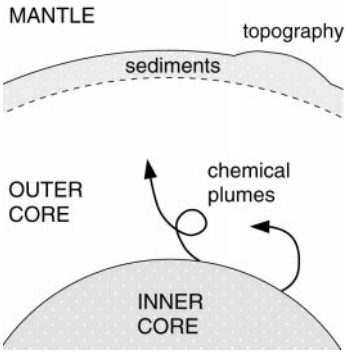

Fig. 2. Schematic cross section of Earth's core and lower mantle. Light elements are segregated into the outer core as the inner core grows by solidification. The increasing concentration of light elements in the outer core causes excess light elements to form sediments, possibly through chemical reactions at the CMB. The sediments accumulate preferentially in depressions at the top of the core. Although compaction of the sediments has the effect of expelling liquid iron and reducing the thickness of the layer, the sediment front (dashed line) moves downward with time.

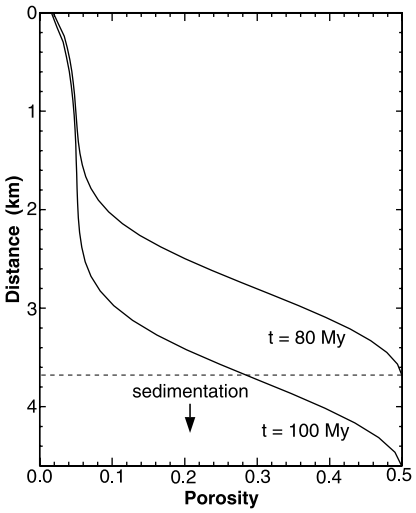

Fig. 3. Profiles of porosity calculated in the sedimentary layer after 80 and 100 My of accumulation. A region of high porosity develops in the lowermost part of the layer where new sediments are added. A region of nearly constant porosity increases in vertical extent as sediments accumulate.

not essential for our discussion. Instead, we treat the initial porosity ϕ_0 at the time of deposition as a model parameter and use analogies with crystal accumulation in magma chambers (*28*) and deposition of seafloor sediments to assign a value of $\phi_0 = 0.5$. The volumetric rate of deposition is then given by $\dot{V}_{sed} = \dot{M}_{sed}/(\rho_{sed}\phi_0)$, where the dot denotes a time derivative. Combining these results gives the deposition rate in terms of the growth of the inner core

$$\dot{V}_{sed} = \Delta C\left(\frac{\rho_c}{\rho_{sed}\phi_0}\right)\left(\frac{m_{sed}}{m_X}\right)\dot{V}_{ic} \qquad (2)$$

where $\dot{V}_{ic} = \dot{M}_{ic}/\rho_c$ is determined using a model for the thermal evolution of the core (*29*). We adopt $\dot{V}_{sed}/\dot{V}_{ic} \approx 1$ as a plausible estimate (*30*) and assume initially that the sediments are uniformly distributed over the CMB.

The density difference between the sediments and liquid iron should cause viscous compaction of the layer. The porosity of the sediments gradually decreases after deposition, and the interstitial liquid iron is expelled. The equations governing viscous compaction are well known (*31, 32*) and have been applied to sedimentation processes in a variety of geological settings (*28, 33*). We apply the formulation of McKenzie (*31*) to quantify the one-dimensional compaction of a plane layer (*34*). The top of the layer rests against the base of the mantle, which we assume is relatively impermeable compared with the permeability of the sediments (Fig. 2). We also assume that the stress on the lower interface of the sediment layer vanishes because the viscosity of the underlying liquid core is negligible compared with that of the silicate matrix (see below). The initial porosity ϕ_0 at the time of deposition is imposed as a boundary condition on the porosity at the lower interface. An important consideration in these calculations is whether the liquid Fe remains interconnected in the silicate matrix. Several lines of experimental evidence (*22, 35*) suggest that liquid Fe wets the surface of silicate minerals at high pressure and temperature. Otherwise, isolated pockets of liquid Fe develop within the layer as the porosity decreases. The lack of evidence for Fe droplets persisting in the mantle after core formation suggests that silicates are permeable to liquid Fe. We characterize the relation between permeability and porosity using the Kozeny-Carman equation (*36*).

A second constitutive equation is required to describe the stress-strain relation in the solid matrix. The resistance of the porous matrix to compaction is characterized by an effective bulk viscosity that is typically comparable in magnitude to the shear viscosity of the solid grains (*31, 32*). On the basis of estimates of the shear viscosity in the lower mantle (*37*), we adopt 10^{22} Pa·s as a nominal value for the bulk viscosity. However, we explore the possibility that higher temperatures at the CMB reduce the bulk viscosity. For the viscosity of liquid iron, we assume a value of 10^{-2} Pa·s (*38*).

The predicted profiles of porosity at two epochs [separated by 20 million years (My)] are shown in Fig. 3. The largest porosity occurs at the interface where the sediments are deposited. The initial value of $\phi_0 = 0.5$ decreases rapidly to a residual value of $\phi \approx 0.05$ over 1.5 km. The structure of porosity near the sedimentation front is almost invariant as the layer advances into the core. Deeper than 1.5 km into the layer, the porosity becomes nearly uniform. In this region the sediment permeability is low enough to inhibit the expulsion of liquid iron. Increases in the liquid pressure develop in response to compaction, which opposes the buoyancy forces and limits further consolidation. The region of nearly uniform porosity extends several kilometers into the layer after 100 My of accumulation.

The general form of the porosity distribution is unaltered by different choices of parameter values, although specific details are affected. For example, the zone of high porosity near the sedimentation front is influenced by the viscosity η_s of the solid matrix and the rate of sedimentation $\dot{V}_{sed}/A_{sed}$, where A_{sed} is the area of sedimentation. Scaling suggests that the vertical extent of this region depends on η_s and $\dot{V}_{sed}/A_{sed}$ in the combination $(\eta_s\dot{V}_{sed}/A_{sed})^{1/2}$. For example, a matrix viscosity of 10^{21} Pa·s reduces the vertical extent of the high-porosity region to about 500 m. On the other hand, reducing A_{sed} by confining sedimentation to topographic depressions in the CMB broadens the high-porosity zone. Further into the sedimentary layer, the value of residual porosity is controlled by the permeability of the sediments. Permeability is a strong function of the grain size a in the Kozeny-Carman equation (*36*). We adopt $a = 10^{-7}$ m as a plausible value, although there are currently no constraints on this parameter. Calculations with other choices of a indicate that the residual porosity is inversely proportional to a. For example, when $a = 5 \times 10^{-7}$, we predict a residual porosity of 1% (versus 5% in Fig. 3).

The vertical extent of the residual-porosity zone increases with accumulation time and can exceed tens of kilometers after several hundred My of accumulation. The iron contained in the residual porosity is eventually buried deep enough to become entrained in mantle convection. This process may explain the enrichment of ^{186}Os and ^{187}Os (relative to ^{188}Os) in some mantle plumes (*39*). The isotopic signatures in primitive Hawaiian picrites are attributed to the addition of 0.5% to 1% core material in the Hawaiian plume, which is compatible with the range of residual porosities obtained in our calculations.

Some physical properties of the sedimentary layer can be estimated using the predicted profiles of porosity. The density is obtained from a volume average of the silicate and iron components, whereas the electrical conductivity is estimated using Archie's law (*40*). The *P*- and *S*-wave velocities v_p and v_s are estimated using the Hashin-Shtrikman upper bounds on the effective elastic moduli, so that our predicted reductions in seismic velocities are minimum values (*41*). The predicted density perturbation relative to $\rho = 5570$ kg m^{-3} decreases from a maximum value of 38% at the sedimentation front to values of 4 to 5% in the region of residual porosity (Fig. 4A). The electrical conductivity is 1.8×10^5 S m^{-1} at the sedimentation front, but decreases rapidly to values of order 10^3 S m^{-1} in the region of residual porosity. The total conductance of the layer is 1.7×10^8 S, which is sufficient to explain the nutation observations (Fig. 4B) (*14, 42*). Our estimates for the elastic velocities suggest that the reduction in *S*-wave velocity (relative to $v_s = 7.26$ km s^{-1}) is about twice as large as the reduction in *P*-wave velocity (relative to $v_p = 13.72$ km s^{-1}) (Fig. 4C).

Both the relative and absolute magnitudes of the *P*- and *S*-wave velocity reductions are large enough to provide a viable explanation for the ULVZ (*6–11*). The thickness of the anomalous zone (coinciding with the region of high porosity) also proves to be sufficient. Waveform modeling using the seismic velocities and density predicted for the sedimentary layer yields the results shown in Fig. 1B. In particular, the appearance of a second peak in the observed seismic record (identified as

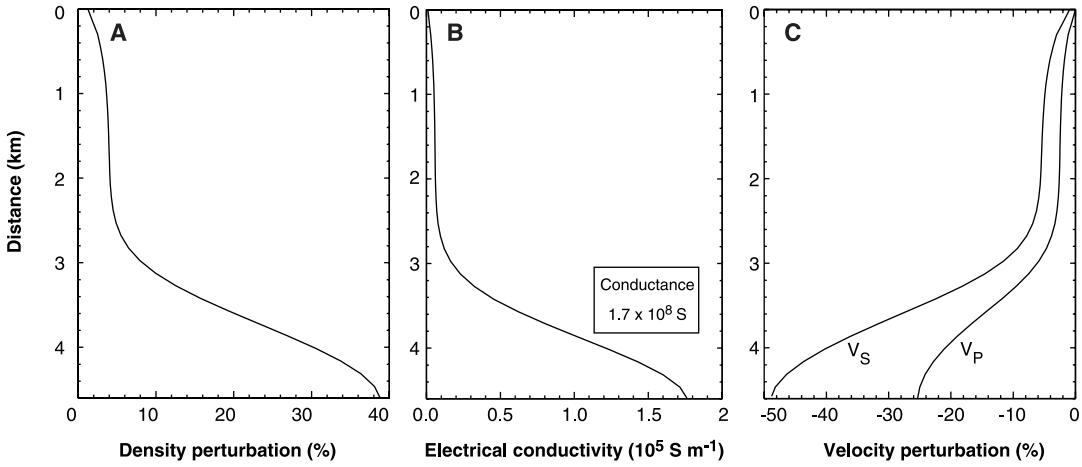

Fig. 4. Physical properties of the sedimentary layer are estimated using the profiles of porosity. (**A**) The density is a volume average of the sediment and liquid iron components. (**B**) The electrical conductivity is calculated using Archie's law (*40*) and assumes that the sediments are electrically insulating. (**C**) The anomalies in *P*- and *S*-wave velocity are estimated using the Hashin-Shtrikman upper bound and are expressed as percentages relative to the average properties of the lowermost mantle.

SP_dKS) is reproduced in the calculated waveform (solid line). Comparable results are obtained using a more typical ULVZ model (dashed line), in which the layer thickness is 5 km and the *P*- and *S*-wave reductions are –10% and –30%, respectively (*9*).

It is unlikely that sediments accumulate uniformly over the surface of the CMB. Instead, sediments would tend to collect in areas where the CMB is displaced into the mantle relative to the average boundary position (topographic highs in the boundary position correspond to basins from the point of view of the core). More rapid accumulation and thicker deposits enhance the elastic perturbations in these areas, so we expect a correlation between the location of ULVZs and positive radial displacements of the CMB. Testing for such a correlation using better maps of the CMB topography and ULVZ locations would afford an important test of our model. Other tests are suggested by the physical structure of the layer. For example, the large reductions in *S*-wave velocity are confined to a 1- to 2-km layer, which is too thin to produce distinct precursors in reflected *S*-waves (particularly *ScP*). Thus, we expect no anomalous *ScP* waves in regions where ULVZs are detected in SP_dKS data (*43, 44*). However, undulations in the top of the sediment layer resulting from entrainment by the mantle could cause focusing (or defocusing) of seismic waves that reflect from the mantle side of the CMB. In contrast, filling of the boundary topography with sediments would reduce the effects of boundary topography on the reflection of seismic waves from the core side of the CMB.

Enrichment of Os isotopes in Hawaiian picrite lavas is compatible with the presence of sediments at the top of the core, but the data do not demand this interpretation. Similarly, seismological evidence for ULVZs does not require a sedimentary layer, although these data can be explained by such a layer. A more stringent constraint comes from observations of Earth's nutation, which appear to require a layer at the base of the mantle with a conductance of 10^8 S. The remarkable agreement between nutation theory and observations restricts alternative interpretations. One possibility requires an increase in the viscosity of the liquid core to 10^3 Pa·s (*13*). However, there is no basis for increasing the current theoretical estimates of viscosity by more than five orders of magnitude (*38*).

Sediments offer a plausible explanation for the conducting layer inferred from nutation observations, and can also account for the ULVZ. This layer may also have important consequences for convection in the core, because the incorporation of light elements into sediments leaves behind a dense iron-rich liquid, which sinks into the interior of the core. This additional source of buoyancy could increase the power available to maintain Earth's magnetic field by a factor of 2 (*45*).

References and Notes

1. T. Lay, Q. Williams, E. J. Garnero, *Nature* **392**, 461 (1998).
2. S. P. Grand, *J. Geophys. Res.* **99**, 11591 (1994).
3. W. J. Su, R. L. Woodward, A. M. Dziewonski, *J. Geophys. Res.* **99**, 6945 (1994).
4. X. D. Li, B. Romanowicz, *J. Geophys. Res.* **101**, 22245 (1996).
5. G. Masters, S. Johnson, G. Laske, H. Bolton, *Philos. Trans. R. Soc. London Ser. A* **354**, 1385 (1996).
6. J. Mori, D. V. Helmberger, *J. Geophys. Res.* **100**, 20359 (1995).
7. E. J. Garnero, D. V. Helmberger, *Geophys. Res. Lett.* **23**, 977 (1996).
8. J. Revenaugh, R. Meyer, *Science* **277**, 670 (1997).
9. E. J. Garnero *et al.*, in *The Core-Mantle Boundary Region*, M. Gurnis *et al.*, Eds. (American Geophysical Union, Washington, DC, 1998), pp. 319–344.
10. Q. Williams, E. J. Garnero, *Science* **273**, 1528 (1996).
11. E. J. Garnero, R. Jeanloz, *Geophys. Res. Lett.* **27**, 2777 (2000).
12. P. M. Mathews, I. I. Shapiro, *Annu. Rev. Earth Planet. Sci.* **20**, 469 (1992).
13. B. A. Buffett, *J. Geophys. Res.* **97**, 19581 (1992).
14. The high-conductivity material must be located at the CMB interface and be immobile relative to flow in the outer core. The layer may be embedded within the lowermost mantle, or (as proposed here) it may have finite rigidity at the top of the core. Nutation observations constrain the conductance of the layer to be 10^8 S or more.
15. T. J. Shankland, J. Peyronneau, J. P. Poirier, *Nature* **366**, 453 (1993).
16. F. Birch, *J. Geophys. Res.* **69**, 4377 (1964).
17. D. J. Stevenson, *Science* **214**, 611 (1981).
18. E. Knittle, R. Jeanloz, *Geophys. Res. Lett.* **16**, 609 (1989).
19. F. Goarant, F. Guyot, J. Peyronneau, J.-P. Poirier, *J. Geophys. Res.* **97**, 4477 (1992).
20. E. Ito, K. Morooka, O. Ujike, T. Katsura, *J. Geophys. Res.* **100**, 5901 (1995).
21. J. Bloxham, A. Jackson, *Rev. Geophys.* **29**, 97 (1991).
22. E. Knittle, R. Jeanloz, *Science* **251**, 1438 (1991).
23. J. M. Brown, R. G. McQueen, *J. Geophys. Res.* **91**, 7485 (1986).
24. Q. Williams *et al.*, *Science* **236**, 181 (1987); R. Boehler, *Nature* **363**, 534 (1993).
25. V. Courtillot, J. L. LeMouël, J. Ducruix, *Geophys. J. R. Astron. Soc.* **78**, 619 (1984).
26. The properties of the silicate sediments are based on the physical properties of the lower mantle. The density $\rho_{sed} = 5570$ kg m^{-3}, *P*-wave velocity $v_{sed}^P = 13.72$ km s^{-1}, and *S*-wave velocity $v_{sed}^S = 7.26$ km s^{-1} are taken from the reference model of A. M. Dziewonski and D. L. Anderson [*Phys. Earth Planet. Inter.* **25**, 297 (1981)]. The molar mass of the sediments, $m_{sed} = 108$ g mol^{-1}, is based on silicate perovskite $(Mg_{0.85},Fe_{0.15})SiO_3$.
27. V. S. Solomatov, P. Olson, D. J. Stevenson, *Earth Planet. Sci. Lett.* **120**, 387 (1993).
28. D. N. Shirley, *J. Geol.* **94**, 795 (1986).
29. To leading order, the radius of the inner core increases with time as $t^{1/2}$. We assume that the inner core grew to its present radius of 1221 km in $\tau = 2 \times 10^9$ years and let $V_{ic}(t) = (t/\tau)^{3/2} V_{ic}(\tau)$.
30. Estimates of the sedimentation rate depend on the composition of the core. One possible composition includes 10 weight percent (wt %) oxygen as FeO [R. Jeanloz, T. J. Ahrens, *Geophys. J. R. Astron. Soc.* **62**, 505 (1980)]. In this case we take $m_X = 16$ g mol^{-1} and $\Delta C = 0.1$, assuming that no light element enters the inner core. Using sediment properties in (*26*), $\rho_c = 9900$ kg m^{-3}, and $\phi_0 = 0.5$, we obtain $\dot{V}_{sed}/\dot{V}_{ic} = 1.35$. An alternative composition is 7.3 wt % silicon ($m_X = 28.1$ g mol^{-1}), 4.0 wt % sulfur ($m_X = 32.0$ g mol^{-1}), and 2.3 wt % oxygen ($m_X = 16$ g mol^{-1}) [C. J. Allegre *et al.*, *Earth Planet. Sci. Lett.* **134**, 515 (1995)]. Adding these three components yields $\dot{V}_{sed}/\dot{V}_{ic} = 1.26$. Allowing for light elements in the inner core would reduce these ratios, so we take $\dot{V}_{sed}/\dot{V}_{ic} \approx 1$ as a representative estimate.
31. D. McKenzie, *J. Petrol.* **25**, 713 (1984).
32. D. R. Scott, D. J. Stevenson, *Geophys. Res. Lett.* **11**, 1161 (1984).
33. I. Sumita, S. Yoshida, M. Kumazawa, Y. Hamano, *Geophys. J. Int.* **124**, 502 (1996).
34. The effects of curvature at the CMB may be safely neglected when the layer is thin.
35. J. P. Poirier, J. L. LeMouël, *Phys. Earth Planet. Inter.* **73**, 29 (1992).
36. The permeability k is related to the porosity ϕ by $k = \phi^3 a^2/[K(1 - \phi)^2]$, where a is the grain size of the

sediments and K is a constant factor. Following (*29*), we let $K = 10^3$, and assume $a = 10^{-7}$ m, which is comparable to the size of typical clay particles.
37. J. X. Mitrovica, A. M. Forte, *J. Geophys. Res.* **102**, 2751 (1997).
38. G. A. de Wijs *et al*., *Nature* **392**, 805 (1998).
39. A. D. Brandon *et al*., *Science* **280**, 1570 (1998).
40. Archie's law defines the electrical conductivity of the porous sediments as $\sigma = \phi^n \sigma_c$, where $\sigma_c = 5 \times 10^5$ S m^{-1} is the electrical conductivity of liquid iron and n is a constant that typically lies between 1 and 2. We choose $n = 1.5$ in our calculations.
41. The *P*- and *S*-wave velocities are based on the Hashin-Shtrikman bounds for elastic composites. We plot the upper bounds so that our velocity reductions represent minimum values. [J. P. Watt, G. F. Davies, R. J. O'Connell, *Rev. Geophys.* **14**, 541 (1976)]. The sediment properties are based on the mantle properties in (*26*). The *P*-wave velocity in the liquid is $v_c^P = 8.06$ km s^{-1}.
42. P. M. Mathews, B. A. Buffett, T. A. Herring, in preparation.
43. E. J. Garnero, J. E. Vidale, *Geophys. Res. Lett.* **26**, 377 (1999).
44. J. C. Castle, R. D. van der Hilst, *Earth Planet. Sci. Lett.* **176**, 311 (2000).
45. The rejection of light elements from the inner core provides an important source of buoyancy for convection in the core. Light elements at the inner-core boundary $r = r_{ic}$ are mixed into the volume of the outer core. The release of gravitational energy is proportional to $\bar{\psi} - \psi(r_{ic})$, where $\psi(r_{ic})$ is the gravitational potential at $r = r_{ic}$ and $\bar{\psi}$ is the average potential over the liquid core. If the excess light elements are subsequently incorporated into sediments at the top of the core $r = r_c$, the total release of gravitational energy is proportional to $\psi(r_c) - \psi(r_{ic})$, which is larger than $\bar{\psi} - \psi(r_{ic})$ by about a factor of 2.
46. Partially supported by NSERC (B.A.B.), NSF, the UC Institute of Geophysics (R.J.), and NSF grants EAR-9905710 and NSF-9996302 (E.J.G.).

22 June 2000; accepted 29 September 2000

Regional Changes in Carbon Dioxide Fluxes of Land and Oceans Since 1980

Philippe Bousquet,[1,2]* Philippe Peylin,[1] Philippe Ciais,[1] Corinne Le Quéré,[1]† Pierre Friedlingstein,[1] Pieter P. Tans[3]

We have applied an inverse model to 20 years of atmospheric carbon dioxide measurements to infer yearly changes in the regional carbon balance of oceans and continents. The model indicates that global terrestrial carbon fluxes were approximately twice as variable as ocean fluxes between 1980 and 1998. Tropical land ecosystems contributed most of the interannual changes in Earth's carbon balance over the 1980s, whereas northern mid- and high-latitude land ecosystems dominated from 1990 to 1995. Strongly enhanced uptake of carbon was found over North America during the 1992–1993 period compared to 1989–1990.

Over the past two decades, on average, about half of the CO_2 emissions caused by fossil fuel combustion have remained in the atmosphere, the rest having been absorbed by the ocean and by land ecosystems. Year-to-year variations in the rate of atmospheric CO_2 accumulation are of the same magnitude as the decadal mean annual accumulation and result primarily from shifts in the natural carbon fluxes (*1*). Previous investigations into which reservoir (land or ocean) and which regions caused such year-to-year changes have produced conflicting answers. Carbon stable isotope studies all infer large shifts of both land and ocean fluxes of up to several gigatonnes (10^{15} g) of carbon per year (GtC year^{-1}) (*2, 3*). In contrast, ocean carbon models and measurements of the CO_2 partial pressure difference between the ocean surface and the atmosphere (ΔpCO_2) suggest relatively small changes in the air-sea fluxes (*4–6*). Global biogeochemical models of the land biosphere generally produce large interannual shifts in terrestrial fluxes, but they differ in where or how they attribute these shifts to underlying processes (photosynthesis or respiration).

Inverse models using atmospheric CO_2 observations and atmospheric transport have been applied to infer the mean spatial distribution of CO_2 fluxes (*7–9*), but rarely to estimate their interannual variability (*10*). Here, we constructed an inversion using 20 years of atmospheric CO_2 measurements, mostly from the NOAA Climate Monitoring and Diagnostics Laboratory air sampling network, to infer monthly changes in the carbon balance of large regions. The carbon balance of continents and oceans can be considered as the sum of two components, a long-term mean net flux (over 20 years) and a monthly varying flux anomaly. In the following, we present and discuss the monthly varying flux anomalies. The results of the inverse approach ("top-down") are compared with predictions of two state-of-the-art global models ("bottom-up") of the carbon fluxes over land ecosystems and oceans.

Over the past 20 years, the annual accumulation of CO_2 in the atmosphere has varied between 1 and 6 GtC year^{-1} (*1*). Because fossil CO_2 emission changes do not vary much from year to year, the observed changes in accumulation rate reflect variations of ocean and land fluxes. At present, about 120 CO_2 data records from around the globe are available (*11*). Most CO_2 stations are in the marine boundary layer; they can be influenced directly by ocean fluxes and more indirectly by land fluxes. A few CO_2 stations, however, are close to or within the continents and can better capture year-to-year changes in terrestrial fluxes. Among the 120 sites available in 1998, we have selected 67 sites (*12*). At each site, we have analyzed the variance of the deseasonalized trend after subtraction of the trend at the South Pole (*13*). This analysis indicates that there is "excess" variance at low frequency at continental sites compared to oceanic sites (Fig. 1). This excess variance may reflect short-term spatial and temporal variability of land fluxes or of atmospheric transport. However, it also suggests that terrestrial carbon fluxes exhibit larger year-to-year variations than their oceanic counterparts. This inference can be evaluated by using an inverse model to calculate regional carbon balance variations from observed concentration variations.

We have developed such a model, extending the work of (*9*), to retrieve the net CO_2 fluxes every month from 1980 to 1998 (*13*). The inverse model optimizes CO_2 ocean and land fluxes for 11 continental regions and eight ocean regions (Fig. 1) by minimizing the differences between the CO_2 concentrations simulated by a three-dimensional atmospheric transport model and those observed at measurement sites. Fossil CO_2 fluxes are prescribed from energy use statistics (*14*). The control inversion is described in (*13*). The atmospheric CO_2 data used for the inversion are calculated from 67 selected monitoring sites (*12*) over the period 1980–1998. Raw flasks and in situ records are smoothed in the time domain to remove synoptic variability (*11*) and are used in the form of monthly means. An increasing number of stations is available over time, from 20 sites in 1980 to 67 sites in 1997, with 35 new sites appearing between 1987 and 1991. Data uncertainties are estimated each month at each station from the (synoptic) scatter and measurement uncertainties of the original flask data (*13*). In addition to the control inversion (*13*), we have carried out a sensitivity study consisting of seven additional inversions in which key parameters are varied individually (*15*), provid-

[1]Laboratoire des Sciences du Climat et de l'Environnement (LSCE), F-91198 Gif-sur-Yvette Cedex, France. [2]Université de Versailles Saint Quentin en Yvelines (UVSQ), F-78035 Versailles Cedex, France. [3]National Oceanic and Atmospheric Administration (NOAA), Climate Monitoring and Diagnostics Laboratory, Boulder, CO 80303, USA.

*To whom correspondence should be addressed. E-mail: pbousquet@cea.fr

†Present address: Max-Planck-Institut für Biogeochemie, D-07701 Jena, Germany.